

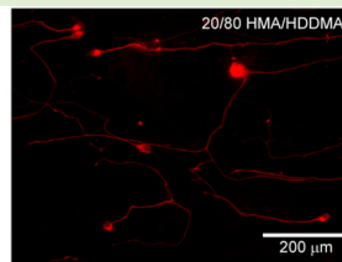
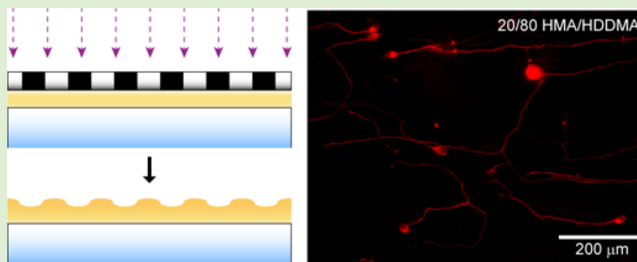
Material Stiffness Effects on Neurite Alignment to Photopolymerized Micropatterns

Bradley W. Tuft,[†] Lichun Zhang,[‡] Linjing Xu,[‡] Austin Hangartner,[†] Braden Leigh,[†] Marlan R. Hansen,[‡] and C. Allan Guymon*,[†]

[†]Department of Chemical and Biochemical Engineering, University of Iowa, Iowa City, Iowa 52242, United States

[‡]Department of Otolaryngology, University of Iowa Hospitals and Clinics, Iowa City, Iowa 52242, United States

ABSTRACT: The ability to direct neurite growth into a close proximity of stimulating elements of a neural prosthesis, such as a retinal or cochlear implant (CI), may enhance device performance and overcome current spatial signal resolution barriers. In this work, spiral ganglion neurons (SGNs), which are the target neurons to be stimulated by CIs, were cultured on photopolymerized micropatterns with varied matrix stiffnesses to determine the effect of rigidity on neurite alignment to physical cues. Micropatterns were generated on methacrylate thin film surfaces in a simple, rapid photopolymerization step by photomasking the prepolymer formulation with parallel line-space gratings. Two methacrylate series, a nonpolar HMA-*co*-HDDMA series and a polar PEGDMA-*co*-EGDMA series, with significantly different surface wetting properties were evaluated. Equivalent pattern periodicity was maintained across each methacrylate series based on photomask band spacing, and the feature amplitude was tuned to a depth of 2 μm amplitude for all compositions using the temporal control afforded by the UV curing methodology. The surface morphology was characterized by scanning electron microscopy and white light interferometry. All micropatterned films adsorb similar amounts of laminin from solution, and no significant difference in SGN survival was observed when the substrate compositions were compared. SGN neurite alignment significantly increases with increasing material modulus for both methacrylate series. Interestingly, SGN neurites respond to material stiffness cues that are orders of magnitude higher (GPa) than what is typically ascribed to neural environments (kPa). The ability to understand neurite response to engineered physical cues and mechanical properties such as matrix stiffness will allow the development of advanced biomaterials that direct de novo neurite growth to address the spatial signal resolution limitations of current neural prosthetics.



INTRODUCTION

The matrix stiffness of native extracellular matrices (ECMs) or synthetic matrices is a key biophysical cue that regulates cellular functions including migration, differentiation, spreading, and proliferation.^{1,2} For example, in a process referred to as durotaxis, NIH 3T3 fibroblast cells are shown to preferentially migrate toward the stiffer substrate on polyacrylamide sheets.³ The number and lengths of angiogenic sprouts from endothelial cells increase with increasing matrix stiffness, which is independent of matrix density.⁴ Furthermore, matrix elasticity significantly affects the cell fate of naive mesenchymal stem cells with soft, stiffer, and rigid matrices that delineate neurogenic, myogenic, and osteogenic cell lineages, respectively.⁵

Neural processes are also known to sense and respond to biophysical cues, including substrate elasticity. For example, primary spinal cord neural processes branch significantly more on softer polyacrylamide gels compared to stiffer matrices.⁶ Additionally, neurites from chick dorsal root ganglia grow significantly longer down a stiffness gradient, that is, harder to softer, than they do up the gradient in a three-dimensional (3D) genipin cross-linked collagen gel.⁷ The behavior of neurons and their processes is of particular interest in cell–material interaction studies, including interactions based on

matrix stiffness, because of their significance in a host of physiological functions. Accordingly, an array of material modifications or microenvironmental controls were developed to influence neuronal behavior, particularly with regard to neurite outgrowth, including the photodegradation of 3D matrices,⁸ diffusion or patterning of bioactive agents,^{9–12} aligned physical features,^{12–17} and electrical fields.¹⁸ These methods are often employed to increase the ultimate unidirectional outgrowth to bridge gaps that are representative of nerve injuries.^{19–22}

Beyond the applications intended to bridge nerve gaps, the ability to understand and control the directionality of de novo neurite growth based on physical material cues may also enable significant functional improvements of current and developing neural prosthetics. Specifically, directing neural processes into closer spatial proximity to stimulating elements of retinal or cochlear implants (CIs) may overcome current spatial signal resolution barriers and enhance prosthesis performance.^{23–27} Furthermore, spatially organized neural growth will likely be

Received: July 14, 2014

Revised: September 8, 2014

Published: September 11, 2014

critical for the high resolution performance of any future device that interfaces with the nervous system.

In this work, we investigate the effects of material mechanical properties, that is, matrix rigidity, on spiral ganglion neuron (SGN) behavior and neurite alignment in response to topographical guidance cues. SGNs are nerve cells in the inner ear that are electrically stimulated by CI prostheses. In a previous work we demonstrated that de novo neurite growth from inner ear SGNs is guided by photopolymerized micropatterns,²⁸ that the extent of the alignment can be tuned based on features dimensions,²⁹ and that response to uni- and multidirectional cues varies significantly even when neurites are presented with similar topographic features.³⁰ For this study, micropatterned thin films are generated for neurite alignment experiments using the spatial reaction control afforded via photopolymerization. UV exposure time is modulated to control the feature depth, which enables a direct comparison of the neuronal and neural process behavior. Two copolymer systems, namely hexyl methacrylate (HMA) with 1,6-hexanediol dimethacrylate (HDDMA) and poly(ethylene glycol) dimethacrylate (PEGDMA) with ethylene glycol dimethacrylate (EGDMA), are used as platforms with different monomer chemistries and for neuronal contact guidance experiments. SGN survival, neurite length, and neurite alignment are compared on substrates that vary in matrix rigidity across each methacrylate series based on changes in the cross-link density. The development of advanced biomaterials that direct de novo neurite growth will require an improved understanding of neuron–material interactions, including the response to substrate stiffness, to improve the spatial signal resolution of existing and future prostheses.

EXPERIMENTAL SECTION

Glass Substrate Functionalization. Methacrylate thin films were polymerized on functionalized glass slides to prevent polymer delamination and facilitate the cellular microscopy studies. Standard microscope glass slides (2.54 cm × 7.62 cm × 0.1 cm) were functionalized with the silane coupling agent 3-(trimethoxysilyl)propyl methacrylate (Aldrich). Prior to treatment with the coupling agent, the slides were first cleaned and oxidized with O₂ plasma for 3 min at 30 W RF power (PDC-001 Harrick Plasma Expanded Cleaner, Ithaca, NY) while under a 300 mTorr vacuum. Following the removal from the plasma chamber, the slides were immersed in a 1/100 v/v solution of the silane coupling agent and *n*-hexane (Aldrich) overnight in a covered container at room temperature (~21 °C). Each slide was then rinsed with fresh hexane and dried in the fume hood before being placed in a sealed container. The functionalized slides were used immediately as substrates for polymerization.

Photopolymerization of Micropatterned Methacrylate Thin Films. All of the mixtures of HMA (Aldrich) with HDDMA (Aldrich) and PEGDMA (Aldrich, $M_n = 600$) with EGDMA (Aldrich) were prepared with 1 wt % of 2,2-dimethoxy-2-phenylacetophenone (DMPA, BASF) as the photoinitiator. Copolymer compositions are represented as whole numbers (e.g., 40/60, 50/50), but each polymer fraction is 0.5 wt % less to account for the photoinitiator. Twenty microliters of prepolymer solutions were pipetted onto the center of a functionalized slide and then covered with a 2.54 cm × 2.54 cm × 0.1 cm glass–chrome Ronchi rule photomask (Applied Image Inc., Rochester, NY) for the parallel patterns or with a cut untreated glass slide of the same dimensions for the unpatterned samples. Capillary forces caused the formulations to spread evenly under the photomasks. Photopolymerization was carried out with a high-pressure mercury vapor arc lamp (Omnicure S1500, Lumen Dynamics, Ontario, Canada) at a 365 nm light intensity of 16 mW/cm². The curing module was equipped with an 8 mm aperture × 50 mm length beam homogenizing fused silica light pipe (Edmund Optics) and a

collimating lens (RLQ-1, Asahi Spectra). The light intensity was measured with a Cole–Parmer Series 9811 radiometer. The microfeature amplitude was tuned by shutting off UV radiation at specific times, which thereby prevented further initiation events and resulted in the rapid termination of the polymerization. Following the set exposure time, the photomask was removed from the polymer, and the sample was washed with 95% ethanol to remove any residual surface monomer. The rinsed samples were then postcured for 10 min using the same light source and intensity without the photomask and under ambient conditions to maximize the monomer conversion.

White Light Interferometry. The micropattern feature spacing and depth were measured by white light interferometry (Dektak Wyko 1100 Optical Profiling System, Veeco). The feature amplitude was measured as the difference between a maximum ridge value and an adjacent minimum groove value. For each composition and exposure time, the average feature height was determined by measuring channel amplitude in nine different areas across the surface ($n \geq 3$). The feature spacing, or periodicity, was measured as the distance between the highest points on adjacent ridges and was consistent with the photomask band spacing. The measurements and 3D images were generated by Vision software associated with the instrument.

Scanning Electron Microscopy. The micropattern morphology of each composition was further characterized by scanning electron microscopy (SEM) (S-4800, Hitachi). Conductive silver paint was applied to the bottom of glass substrates modified with micropatterned methacrylate thin films for mounting on aluminum SEM stubs to acquire the top-down images. For the cross-sectional images, a glass etcher was used to etch the sample on the side opposite the thin polymer film, and patterned polymers were then fractured and mounted vertically on the specimen stages. The SEM specimen stage was rotated using automated stage and software controls. Each polymer surface was sputter coated with gold prior to examination by SEM. The electron accelerating voltage was set at 2 kV.

Cell Culture. The polymer substrates attached to glass slides were sterilized with 70% ethanol and UV irradiation and air-dried in a culture hood. The micropatterned surfaces were then coated sequentially with poly-L-ornithine (100 µg/mL) at room temperature and laminin (20 µg/mL) at 4 °C overnight. The following day, dissociated spiral ganglion (SG) cultures from P3–6 rat pups were prepared as previously described.^{31,32} The dissociated cultures were plated with equal volumes of the cell suspension and maintained in a humidified incubator with 6.5% CO₂ for 48 h. The cultures were maintained in Dulbecco's Modified Eagle Medium (DMEM) supplemented with N₂ additives, insulin, 5% fetal bovine serum, neurotrophin-3 (NT-3) (50 ng/mL), and brain-derived neurotrophic factor (BDNF) (50 ng/mL).

Immunostaining and Measurement of SGN Survival and Neurite Length. The SGN cultures were fixed with 4% paraformaldehyde at 4 °C for 20 min, permeabilized and blocked with 5% goat serum, 2% bovine serum albumin (BSA), 0.1% Triton X in phosphate buffered saline (PBS), and immunostained with antineurofilament 200 (NF200) antibodies (1:400, Sigma-Aldrich) at 37 °C for 2 h, as previously described.³¹ Alexa 488 conjugated secondary antibody (1:800, Invitrogen) was used to detect the primary antibody immunolabeling at room temperature for 1 h. The slides were treated with ProLong Gold antifading reagent with DAPI (Life Technology) and sealed with nitrocellulose. The digital epifluorescent images were captured of the entire polymer surface using the scan slide application of the Metamorph software (Molecular Devices, Silicon Valley, CA) on a Leica DMIRE2 microscope (Leica Microsystems, Bannockburn, IL) with a Leica DFC350FX digital camera. The total number of NF200-positive neurons with healthy nuclei was counted from the digital images for each polymer surface to determine the SGN survival. The SGN survival on each polymer was expressed as the percent survival relative to the number of SGNs in the cultures maintained on tissue culture plastic as previously described.^{33,34} Overall, SGN survival is typically ~25% in cultures maintained on laminin-coated tissue culture plastic.³³ The experiments were performed in duplicate and repeated at least three different times. Neurite length was determined by measuring the longest process of

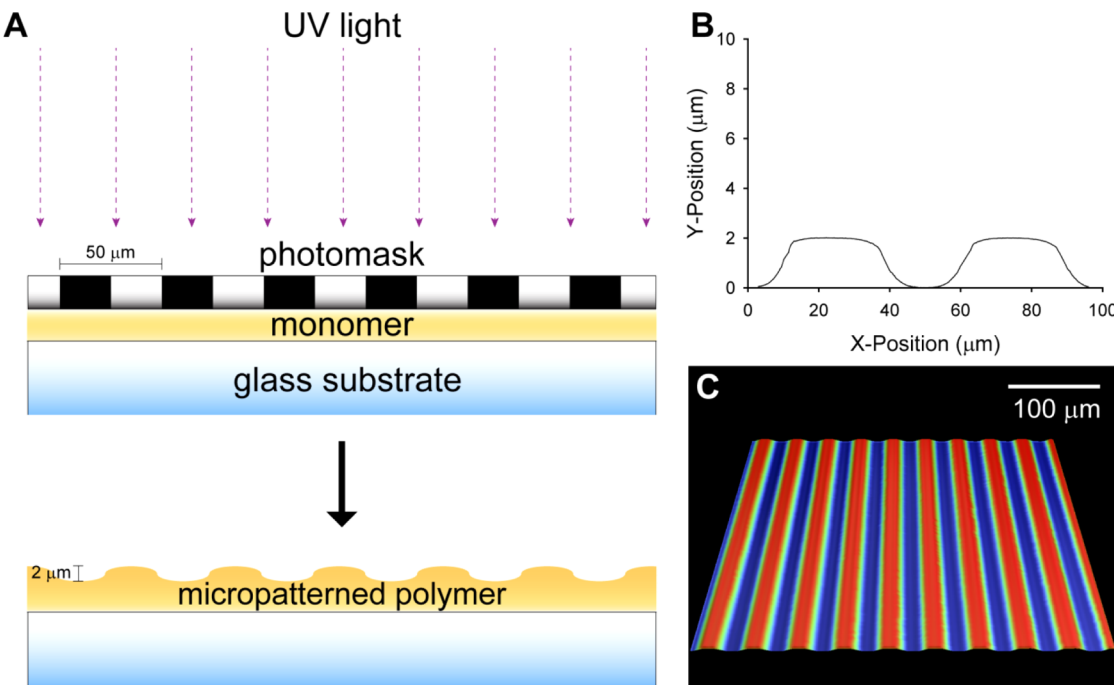


Figure 1. Photopolymerization of micropatterns on methacrylate thin film surfaces. (A) UV exposure of the prepolymer formulation is selectively blocked with a photomask to alter the local reaction kinetics on the surface that result in raised or depressed microfeatures. (B) 2D profile of a 50/50 PEGDMA-*co*-EGDMA ridge–groove–ridge transition generated by white light interferometry. (C) 3D representation obtained by white light interferometry of a micropatterned methacrylate surface formed during a masked photopolymerization. All patterns used for this study have a 50 μm periodicity and a channel amplitude of 2 μm.

100 randomly selected neurites from each slide using the measurement tool in ImageJ (NIH, Bethesda, MD) as previously described.³⁵

Protein Adsorption on Methacrylate Thin Films. Polymer substrates were sequentially coated with poly-L-ornithine (100 μg/mL) at room temperature and 10 μg laminin (20 μg/mL, 0.5 mL in Hank's Balanced Salt Solution, Life Technologies) at 4 °C overnight. The laminin solution was removed by pipet, and the surfaces were washed three times. An equal volume of radioimmunoprecipitation assay (RIPA) buffer containing 50 mM tris(hydroxymethyl)aminomethane (Tris)-HCl, 1% NP-40, 1% Triton X-100, 150 mM NaCl, and 1 mM ethylenediaminetetraacetic acid (EDTA) was applied to each slide to dissolve the adsorbed protein. A 96-well plate protein assay kit (Life Technologies) was used to quantify the protein concentration according to the manufacturer's protocol. Experimental samples and solutions of protein standards with known concentrations were pipetted into the microplate wells and 1x dye reagent was added to each well, mixed, and incubated at room temperature for 5 min. The absorbance was measured by a microplate reader (THERMOmax, Molecular Devices). A standard curve was generated using the absorption values from the protein standards. The protein concentration of the experimental samples was calculated based on the standard curve. Each condition was performed in triplicate and then repeated at three different times.

Contact Angle Measurements. Water contact angles were measured on unpatterned surfaces for each polymer composition using a sessile drop method at room temperature (~21 °C) with a Ramé-Hart NRL 100–00 goniometer (Ramé-Hart Instrument Co., Mountain Lakes, NJ). For each composition, three samples were analyzed with repeats in six different spots for a total of 18 measurements per composition. Drops of doubly distilled H₂O were dispensed as 1 μL volumes.

Measurement of Substrate Rigidity. Tensile tests were performed with a dynamic mechanical analyzer (DMA) (Q800 DMA, TA Instruments) to measure the Young's modulus of each composition as a measure of relative substrate rigidity encountered by neural tissue. The characterization of material moduli enables the comparison of neural pathfinding within a given polymer series. The

polymer specimens for tensile tests were prepared by injecting prepolymer formulations between two untreated glass plates separated by 280 μm thick spacers and held together with clamps. The sample was then irradiated for 10 min using the same lamp and intensity used to fabricate micropatterned surfaces. The polymer bars, with dimensions of 25 mm × 6.4 mm × 0.28 mm, were placed in a vertical film tension clamp for the tensile tests. Young's modulus was evaluated at 30 °C using the controlled force tensile mode with a designated force rate (0.5 N/m). The modulus was calculated from the slope of the stress–strain curve in the early linear regime (less than 5% strain) ($n = 5$).

Determination of Neurite Alignment. The neurite alignment to the micropatterns was measured by determining the ratio (T_L/A_L) of the total neurite length (T_L) to the aligned length (A_L). A_L is defined as the distance in a straight line along the direction of the micropattern (set horizontally) from the cell body to the nerve terminus. Neurites that closely follow the pattern have a ratio close to unity (1). Wandering neurites that do not strongly align to the pattern have higher ratios. For each slide, the neurite alignment was measured for 100 randomly chosen SGNs.

Statistics. A statistical analysis was performed using SigmaStat 3.5 software (Systat Software, Chicago, IL). The groups were compared by performing a one-way analysis of variance (ANOVA) followed by a post-hoc Kruskal–Wallis analysis of variance on ranks and a Dunn's Method or Tukey Test multiple comparison procedure. The results were considered statistically significant if $p < 0.05$.

RESULTS AND DISCUSSION

UV Curing of Micropatterned Methacrylate Substrates. The spatial control inherent to radiation curing was used to generate microscale biophysical cues suitable for neural process contact guidance. Specifically, prepolymer methacrylate monomer and photoinitiator mixtures were selectively exposed to UV irradiation through photomasks, which have alternating reflective and transparent 25 μm wide bands (Figure 1). The exposure of the prepolymer formulation to the UV radiation in

this manner modulates local polymerization kinetics, which results in raised or depressed topographic features under transparent or reflective bands, respectively.^{36,37} Propagation proceeds rapidly beneath the transparent bands during UV exposure, which locally increases the polymer chain concentration while depleting the unreacted monomer content. A concentration gradient occurs locally at the interface between the masked and exposed regions of both the monomer and polymer chains. Because unreacted monomer is much smaller than the propagating polymer chains, it diffuses more rapidly into the developing cross-linked network and swells the features during amplitude formation. While polymerization occurs most rapidly under transparent bands, the photomasked regions still undergo polymer formation, albeit more slowly, because of the angled diffraction of light as it passes through narrow slits and because of the diffusion of active species into the shadowed region as well as photon reflections within the system. As a result, a pattern of gradually transitioning microridges and grooves of uniform width and amplitude rapidly develop across the substrate surface in a single fabrication step. Gradual transitions between topographic features are caused by light diffraction as it passes through the microscale photomask bands^{38,39} and are due to monomer diffusion to reactive regions as has been demonstrated in interference patterning holographic photopolymerization.⁴⁰ We previously demonstrated that this size scale is relevant to SGNs, their processes, and associated glial cells.²⁹ Furthermore, hair cell spacing within the cochlea is also within the feature spacing range that is relevant for a future application to improve patient integration with a cochlear prosthetic.⁴¹ The glass substrates used were first oxidized with O₂ plasma and treated with a methacrylated silane coupling agent to improve thin film adhesion and prevent polymer delamination during the neurite microscopy studies.

Many cell-contact guidance studies for neurons and other cell types use microfeatures generated directly by photolithography or indirectly via soft lithography casting over etched silicon masters.^{42,43} For example, human corneal epithelial cells were shown to align to and migrate in the direction of the nanotopography generated by X-ray lithography and reactive ion etching.⁴⁴ Bovine aortic endothelial cells exhibited contact guidance to micropatterned polyacrylamide gels that were fabricated via soft lithography on a patterned silicon master template.⁴⁵ Furthermore, in an effort to produce cartilage tissue engineering constructs that yield superior mechanical properties of the resultant tissue, micropatterned collagen-glycosaminoglycan membranes were generated using a combination of photolithography and softlithography to direct mesenchymal stem cell growth and ECM formation.⁴⁶ As an alternative patterning method, the direct micropattern fabrication by photopolymerization presented here is advantageous as it requires one principle reaction step, few reagents, and simple and inexpensive equipment. By contrast, the generation of micropatterns by photolithographic methods often requires a multistep process, hazardous reagents, expensive substrates, and processing equipment. Furthermore, the creation of a range of gradually transitioning features with direct photopolymerization enables the tailored probing of cell contact guidance behavior in response to simultaneous physical and chemical guidance cues. Sharp features generated with traditional photolithography would likely dominate the cellular interactions, which may mask the effects of bioactive signaling on cellular behaviors. The direct photopolymerization of microfeatures is, therefore, an additional and advantageous tool for the rapid and facile

development of surface active substrates for cell-material interaction studies.⁴⁷

Matching Microfeature Amplitude Across Different Monomer Chemistries. To determine if the SGN neurite response to matrix stiffness is system-dependent, photopolymerized micropatterns were generated on the surfaces of various compositions of two different methacrylate platforms (Figure 2). The HMA-*co*-HDDMA system is a relatively

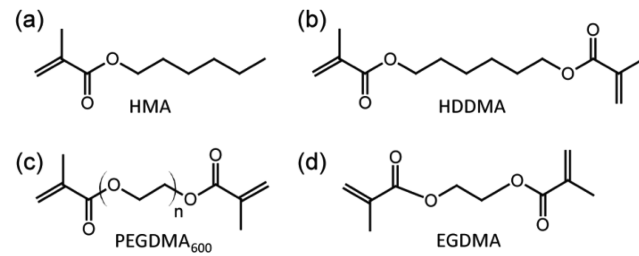


Figure 2. Chemical structures of the monomers used for the micropattern fabrication. Shown are (a) HMA, (b) HDDMA, (c) PEGDMA ($M_n = 600$), and (d) EGDMA.

nonpolar material, and HDDMA serves as the cross-linker. The cross-linking density increases when the HDDMA content increases, which stiffens the material. The PEGDMA-*co*-EGDMA system, by contrast, has a higher surface energy and is more wettable than the HMA-*co*-HDDMA system because of the repeating polar ether linkages between the polymerizable methacrylate moieties on the high molecular weight PEGDMA monomers. Both monomers in the PEGDMA-*co*-EGDMA system undergo cross-linking within the network; however, the cross-linking density decreases when the PEGDMA content increases because of larger spacing between the polymerizable groups, and hence, fewer cross-links per unit volume.

For both of the methacrylate systems, changes in the diene concentration and monomer chemistry alter the polymerization kinetics, which directly affects the formation of the microfeatures on the substrate surface as a function of time. Consequently, the temporal control enabled by photopolymerization, that is, the simple shuttering of the irradiation source at specific exposure times, is crucial to create comparable microfeatures on materials with different monomer chemistries. For a typical radical chain photopolymerization, the shuttering of the light source in this manner prevents the generation of new radical species for initiation events, which significantly precludes further polymerization. To utilize the temporal reaction control thus afforded, specific feature amplitudes were kinetically captured that develop at different exposure times for each composition to create microfeatures with the same amplitude for each polymer composition (Figure 3).

For example, under the given photopolymerization conditions, a microfeature amplitude of 2 μm for the HMA-*co*-HDDMA series occurs at approximately 93, 105, and 114 s for 20, 30, and 40 HMA wt % compositions, respectively. Accordingly, the microfeature amplitude for all compositions was tuned by modulating the UV exposure time based on the reaction kinetics of the prepolymer formulations to generate comparable micropatterns. For the HMA-*co*-HDDMA polymers, the amplitude development profile shifts to higher polymerization times with a decreasing cross-linker content. However, for the PEGDMA-*co*-EGDMA system, the amplitude profile, including the UV exposure time at the maximum amplitude and the subsequent leveling off at a lower amplitude,

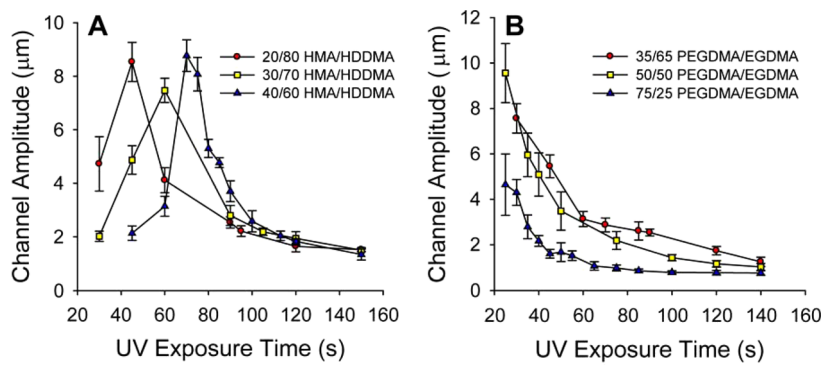


Figure 3. Micropattern feature height is tuned by modulating the UV exposure time as determined by white light interferometry. (A) HMA-*co*-HDDMA amplitude profiles for various compositions and exposure times. Maximum channel amplitudes are similar but occur at earlier polymerization times with the increased diene concentration. (B) PEGDMA-*co*-EGDMA amplitude profiles for various compositions and exposure times. Maximum amplitudes occur early in the reaction because of the rapid vitrification caused by the polymerization of the high molecular weight PEGDMA monomers. Final amplitudes level off at similar heights of approximately $1.5 \mu\text{m}$ for both series. Each composition was masked with a $50 \mu\text{m}$ periodicity glass–chrome photomask and was mixed with 1 wt % DMPA as the photoinitiator. Error bars represent the standard deviation (SD).

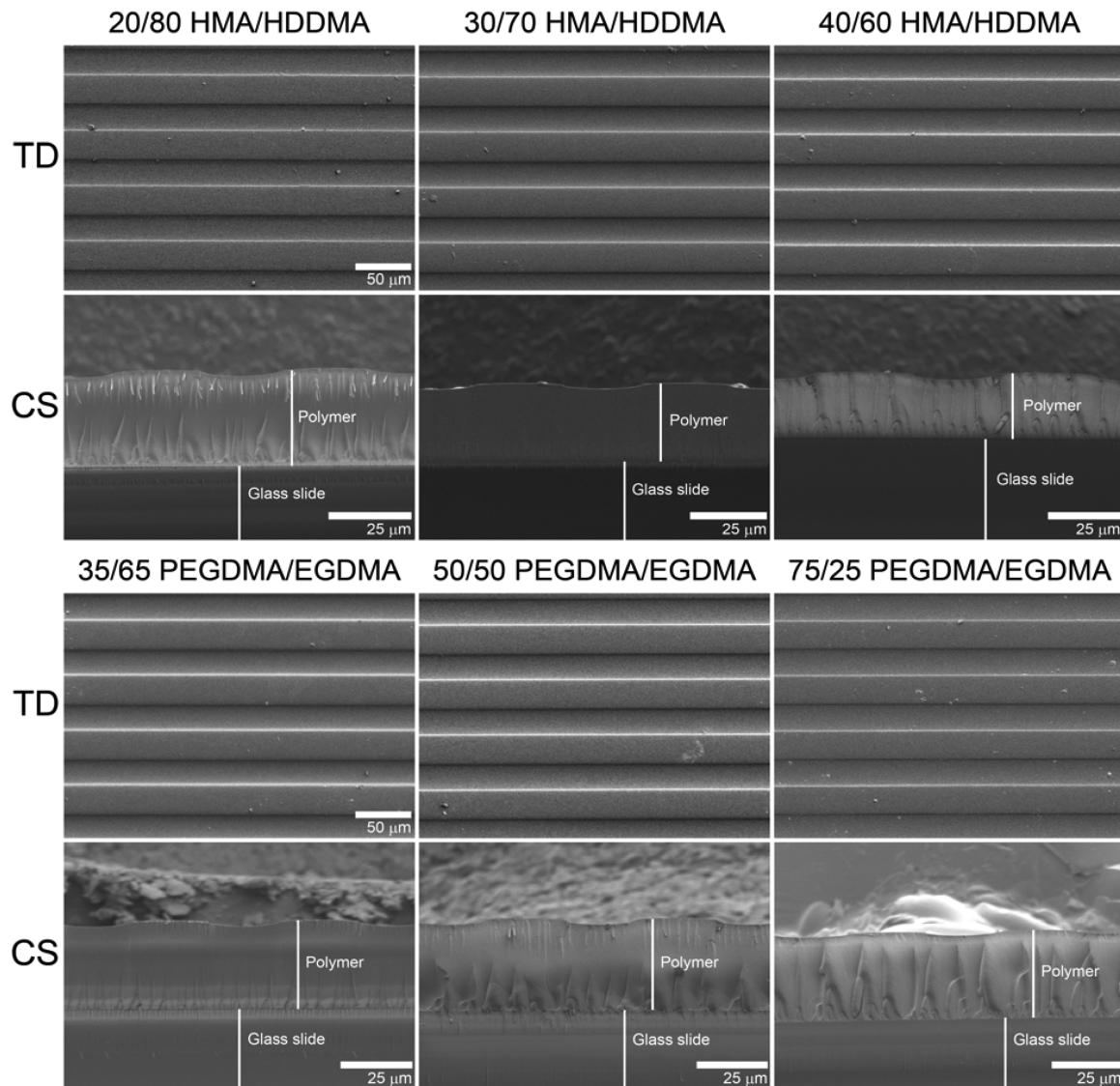


Figure 4. Representative top-down (TD) and cross-section (CS) scanning electron micrographs of the micropatterned polymer surfaces of each methacrylate composition.

occurs at much earlier polymerization times because of the rapid onset of system vitrification caused by the greater

concentration of cross-linking monomers. As a result, the exposure times required to reach a microfeature target

amplitude of 2 μm are much shorter than those for the HMA-*co*-HDDMA system and are reached at 40, 74, and 95 s for 35, 50, and 75 wt % PEGDMA, respectively. For the HMA-*co*-HDDMA system, 2 μm amplitude features were targeted with UV exposure times that occurred after the development of the maximum amplitude.

SEM was used to confirm the white light interferometry measurements and to enable a more detailed comparison of the micropattern morphology of each methacrylate composition (Figure 4). The temporal control of photopolymerization was utilized to generate the 2 μm amplitude features for all of the compositions to allow for simple comparisons of the neurite behavior between systems based on the material mechanical properties rather than on the microfeature dimensions. The microfeature band spacing of the ridges and grooves for all of the compositions closely matches the periodicity of transparent and reflective bands of the photomask with ridge–ridge spacing on the polymersurface, which occur 50 μm apart. Furthermore, the SEM cross-sectional images demonstrate that the polymer film thickness, surface micropatterns, and feature transitions are nearly identical for each composition. The microfeature similarities for the different polymer chemistries indicate that the final surface morphology is strongly shaped by the constraints of the photopolymerization, including light diffraction and reactive species diffusion considerations. Accordingly, the neurite alignment to topographic features would be expected to be nearly identical if only the dimensions of the physical cues, but not the mechanical properties of the substrate, are considered as the contact guidance factors.

Material Surface Chemistry and Adsorbed Adhesive Protein.

To isolate the effect of the matrix rigidity on the neurite alignment to physical micropatterns, we first quantified the surface wettabilities and adsorbed protein contents of HMA-*co*-HDDMA and PEGDMA-*co*-EGDMA to determine their contributions, if any, to differences in neural behavior (Figures 5 and 6). Unpatterned thin films for each methacrylate composition were photopolymerized using the same reaction conditions as outlined for the micropatterned substrates. In place of a photomask, plain glass slides were cut to similar dimensions as the photomasks and used to enable the absorption of full incident light intensity across the entire thin film area. Following the removal of any residual surface monomer with an ethanol wash, the unpatterned polymer surface polarity was quantified by measuring the water contact angles using a sessile drop method (Figure 5). For the HMA-*co*-HDDMA series, the surface becomes slightly more hydrophobic with the increasing HMA content with static water contact angles of $73.8^\circ \pm 1.1$, $76.7^\circ \pm 1.6$, and $79.2^\circ \pm 1.4$ for 20, 30, and 40 wt % HMA, respectively. However, while the contact angle difference between the 20 and 40 wt % HMA compositions is significant, it is unlikely that such a small absolute change in the surface polarity, that is, $\sim 5^\circ$ water contact angle change, would lead to significant differences in neural behavior on the surface. For example, the endothelial and epithelial cell adhesion on OH-, COOH-, and NH₂-terminated self-assembled monolayers does not significantly change within a 5° range, but it does change significantly with larger differences (e.g., 20–80°) in the surface wettability.⁴⁸ Furthermore, it was illustrated that iridium oxide substrates with relatively broad distributions of surface energies are suitable for both insect and vertebrate neuronal growth.⁴⁹

Similar to the HMA-*co*-HDDMA system, the surface polarity does not substantially change across the PEGDMA-*co*-EGDMA

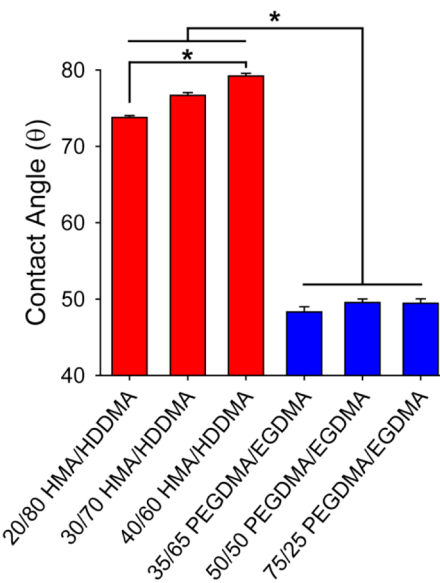


Figure 5. Static water contact angle on unpatterned methacrylate substrates. Surface polarity increases slightly when the HMA concentration increases for the HMA-*co*-HDDMA series with a 5° difference between the 20 and 40 wt % compositions. No statistical difference in the contact angles is observed across the PEGDMA-*co*-EGDMA series. The PEGDMA-*co*-EGDMA series is substantially more polar and wettable, with an average contact angle 30° lower than that of the other methacrylate series (*, $p < 0.05$ one way ANOVA, Dunn's Method). Error bars represent the SD.

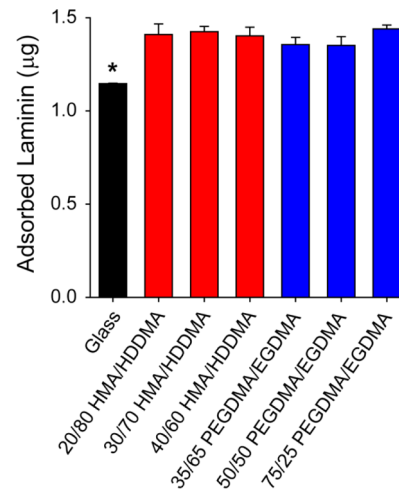


Figure 6. Laminin adsorption on the methacrylate thin films. Laminin adsorption is no different on the nonpolar HMA-*co*-HDDMA substrates than on the polar PEGDMA-*co*-EGDMA substrates. The glass control adsorbed less laminin from solution than did the methacrylate films. (*, $p < 0.05$ one way ANOVA, Tukey Test). Error bars represent the standard error of the mean (SE).

series, with static water contact angles of $48.3^\circ \pm 2.9$, $49.5^\circ \pm 1.8$, and $49.4^\circ \pm 2.5$ for 35, 50, and 65 wt % PEGDMA, respectively. While little to no change in the surface polarity occurs for a given series, a significant difference in the surface polarity is observed when both series are compared. The PEGDMA-*co*-EGDMA series is significantly more polar, that is, wettable, with average static water contact angles $\sim 30^\circ$ lower than those of the HMA-*co*-HDDMA series. Both polymer series have surface polarities that are known to support cellular adhesion and survival.^{50,51} The two platforms, therefore,

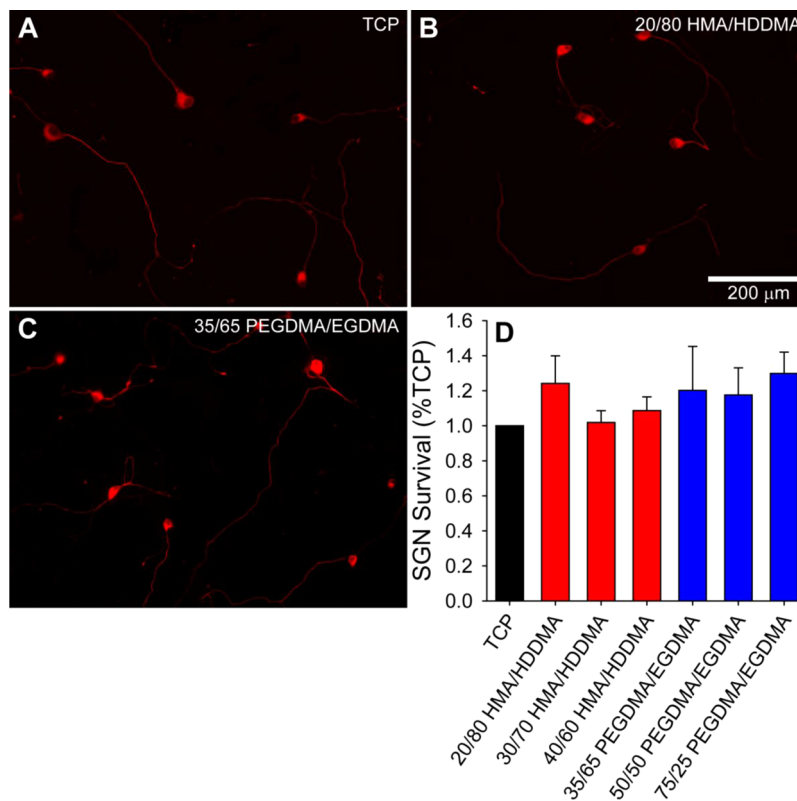


Figure 7. SGN survival on unpatterned TCP and methacrylate thin films. Immunofluorescent images of de novo neurite growth from dissociated SGNs illustrate random neurite outgrowth on the (A) unpatterned TCP and on the unpatterned (B) HMA-*co*-HDDMA and (C) PEGDMA-*co*-EGDMA films. (D) SGN survival on various polymer surfaces is expressed as percent survival on TCP. No significant difference in SGN survival is observed when cultured on HMA-*co*-HDDMA substrates compared to on PEGDMA-*co*-EGDMA substrates. SGN survival on polymer substrates is also similar to the survival on a TCP control ($p = 0.125$, one way ANOVA). Error bars represent the SE.

provide surfaces with substantially different chemical properties but identical microfeature dimensions on which to probe neurite response to material stiffness in relation to topographic cues.

In addition to substrate polarity, the amount of adsorbed laminin on each composition was also measured to determine its potential effects on the neural outcomes including survival, neurite length, and neurite alignment (Figure 6). Laminin is an extracellular glycoprotein that facilitates neuronal adhesion, survival, and neurite growth.⁵² Glycoproteins are polypeptides, that is, proteins, that have covalently attached oligosaccharide side chains. A complex variety of pendant groups populate the main polypeptide chain that includes aliphatic, polar, and charged groups for electrostatic interactions at neutral pH. Pendant surface moieties largely determine the interfacial interactions with material surfaces, which can vary based on the material chemical properties;⁵³ however, even with the substantial disparity in surface polarity between the two methacrylate platforms, no significant difference in the concentration of adsorbed laminin is observed. Furthermore, the adsorbed protein content for each composition across a given series is also nearly identical.

The protein adsorption on varied thin film compositions is likely similar for several reasons. For example, both surface types are moderately wettable, that is, they each have a 40–70° water contact angle, so it is probable that sufficient protein–surface interactions occur with either series to facilitate adhesion. Additionally, while the surface polarity between the two series is substantially different, the functional groups

presented by each material are quite similar. Both series present aliphatic backbones of polymer chains that make up the cross-linked network along with polar ester bonds from the polymerizable methacrylate groups. The main difference in polarity between the two series is due to the presence of the repeating polar ether bonds between cross-links in the PEGDMA-*co*-EGDMA platform. Approximately ten percent of the laminin in solution remains adsorbed to the micro-patterned methacrylate platforms following the rinsing steps, which is similar to but slightly higher than the amount adsorbed on the glass control. This increase is likely due to greater hydrophobic interactions between the protein and the polymer surface compared to the interactions with a highly polar glass substrate. The laminin function is not compromised following the surface adsorption as verified by the healthy outcomes of the dissociated neuronal cultures on each composition, which is indicative of an active surface protein. With little to no change in the surface polarity across either series, and because the adsorbed functional laminin content for each composition is similar, a more direct comparison of the stiffness effects on neurite alignment to physical features can be realized.

SGN Survival and Neurite Growth on Methacrylate Platforms. Dissociated SGNs were cultured on a series of methacrylate substrates with varied matrix stiffnesses in the MPa–GPa range to compare the neuronal and process behaviors. The matrix stiffness is modulated by varying the cross-link density by either increasing the cross-linker concentration in the HMA-*co*-HDDMA series or by tuning the spacing between cross-links based on the high molecular

weight monomer concentration in the PEGDMA-*co*-EGDMA series. As an initial comparison of neural behavior, SGN survival was quantified on a tissue culture plastic (TCP) control and on each micropatterned methacrylate thin film composition (Figure 7). The TCP control and polymer substrates were coated with poly-L-ornithine and laminin to facilitate neuronal adhesion. For both the TCP and unpatterned methacrylate polymers, de novo neurite growth extended randomly across the substrate surface (Figure 7A–C). The SGN survival on the micropatterned methacrylate substrates is comparable to the survival on the TCP control. Furthermore, the SGN survival is not significantly different on the HMA-*co*-HDDMA substrates compared to the PEGDMA-*co*-EGDMA substrates or between the substrates of the same series but with varied matrix stiffnesses (Figure 7D). Similar survival and culture behavior outcomes for SGNs on each methacrylate composition facilitate the comparisons of the neural behaviors, including neurite length and alignment in response to physical cues, without potential complications to account for unhealthy neurons or irregular morphologies. No trend or correlation is observed between SGN survival and methacrylate matrix rigidity under the range of stiffnesses studied.

To compare neurite behavior in response to varied matrix stiffnesses, the SGN neurite length was quantified from the dissociated neuronal populations cultured on micropatterned polymers for each methacrylate composition (Figure 8).

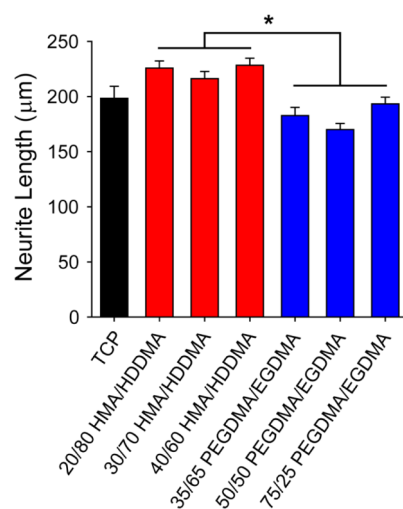


Figure 8. SGN neurite length on the micropatterned methacrylate thin films. Neurite length is significantly shorter on the PEGDMA-*co*-EGDMA substrates compared to the HMA-*co*-HDDMA substrates. The average difference in length between the two series is 40 μm . No significant difference in neurite length is observed between the TCP control and polymer substrates (*, $p < 0.05$, one way ANOVA, Dunn's Method). Error bars represent the SE.

Comparable microfeature spacing and depth are developed for each methacrylate composition using the spatiotemporal control of photopolymerization to allow for direct comparisons of the neural process behavior. Specifically, feature spacing is controlled by photomasking the prepolymer formulation during UV exposure. All of the compositions were selectively blocked with photomasks that had repeating 25 μm reflective, -25 μm transmissive bands, or a 50 μm periodicity. The widths of the photopolymerized microfeatures for all of the compositions closely match the photomask band spacing as observed by

interferometry and SEM. The feature depth is modulated by controlling the irradiation exposure time (Figure 3).

Similar to neuronal survival, no significant difference is observed between the neurite length on the TCP compared to the neurite length on each of the polymer compositions. The SGN survival and neurite length results further illustrate that the photopolymerized methacrylate platforms are amenable to neuronal cultures and that no substantial deviations from typical dissociated SGN culture behavior occur. Furthermore, the neurite lengths on varied compositions of a given series are also similar, which indicates that matrix rigidity does not significantly influence the rate of neurite outgrowth, at least for the range of stiffnesses studied.

Other studies have reported differences in neurite length based on the mechanical properties of the culture material in certain stiffness ranges. For example, neurites from PC12 cells are longer on stiff polydimethylsiloxane (PDMS) substrates (1.72 MPa) than on soft substrates (5 kPa) during the first 5 days of culture.⁵⁴ On the other hand, dorsal root ganglia grow longer neurites in very soft (0.5 kPa) elastin-like polypeptide hydrogels than they do on stiffer (2 kPa) gels.⁵⁵ Furthermore, neurite outgrowth is longer from the neuroblast Neuro-2A cells on stiff matrices (800 kPa) than they are on softer substrates (200 kPa).⁵⁶ However, each of these studies examines the neural response to materials that are orders of magnitude less rigid, that is, in the kPa range, than those that were examined here.

Neurite length may not be significantly influenced after a certain threshold of material stiffness is reached.⁵⁷ Additionally, the neurite length response to matrix stiffness may also be dependent on the neuronal type.

While no substantial difference in neurite length is observed between the TCP control and either methacrylate series, the neurite length is significantly different when both polymer platforms are directly compared. On average, the neurites are approximately 40 μm longer on the HMA-*co*-HDDMA substrates than on the PEGDMA-*co*-EGDMA substrates when maintained under the same culture conditions for the same length of time. Neurite length differences can likely be attributed to increased interactions of the advancing neural growth cones on laminin-coated PEGDMA-*co*-EGDMA polymers compared to laminin-coated HMA-*co*-HDDMA constructs. Because the two polymer series have significantly different surface polarities, it is possible that laminin, while adsorbing at similar surface concentrations (Figure 6), is presented in a more favorable orientation for trans-membrane receptor binding, which increases neurite–substrate interactions and may slow outgrowth. Furthermore, changes in the ECM organization and cell membrane response to material surface energy may also contribute to the observed difference in neurite length.

SGN Neurite Alignment on Micropatterned Substrates with Varied Matrix Stiffnesses. To determine the effect of the rigid matrix stiffness on neurite alignment to physical cues, the cross-link density of each methacrylate platform was modulated while the microfeature periodicity and amplitude were maintained across each composition. For the HMA-*co*-HDDMA series, the matrix stiffness increased by raising the concentration of the dimethacrylate monomer, HDDMA, which increased the cross-link density of the network (Figure 9A). However, when the concentration of the diene increased, the polymerization rate also increased and led to a faster onset of gelation, which alters the microfeature formation

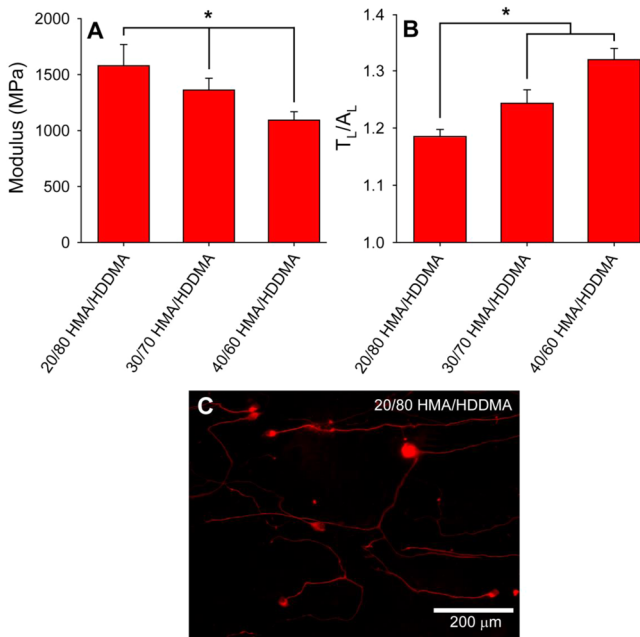


Figure 9. Modulus and SGN neurite alignment on the HMA-*co*-HDDMA series. (A) Material modulus significantly increases with increasing cross-linker concentration (*, $p < 0.05$, one way ANOVA, Tukey Test). Error bars represent the SD. (B) SGN neurite alignment on the micropatterned HMA-*co*-HDDMA substrates. Neurite alignment significantly increases (i.e., alignment ratio T_L/A_L decreases) with increasing substrate stiffness (*, $p < 0.05$, one way ANOVA, Dunn's Method). (C) Representative immunofluorescent image of SGN neurite growth on the micropatterned HMA-*co*-HDDMA polymers. Neurite outgrowth orients to the pattern direction that is set horizontally during the alignment measurement. Error bars represent the SE. The micropattern for each composition has a 50 μm periodicity and a 2 μm amplitude.

time. Accordingly, the UV exposure time must be adjusted to enable the targeting of specific microfeature amplitudes for each composition (see Figure 3). Following the photomasked exposure and subsequent ethanol wash, all of the micropatterned samples were treated with a 10 min post cure to maximize the double bond conversion under the given reaction conditions. While equivalent microfeature spacing and amplitude were maintained for each HMA-*co*-HDDMA composition, the SGN neurite alignment to micropattern features significantly increased with the increasing matrix stiffness (Figure 9B). Specifically, the micropattern periodicity and amplitude were tuned to 50 μm and 2 μm , respectively, using the spatial and temporal control inherent to photopolymerization. Furthermore, the topographic features for each polymer composition, including feature transitions, are not significantly different for both methacrylate series as demonstrated by SEM (Figure 4). The modulation of photopolymerization parameters to precisely tune the topographic features for each composition enables a direct comparison of neurite contact guidance behavior based on material mechanical properties. Neurite alignment ratios (T_L/A_L) approaching unity indicate substantial alignment to the pattern direction along the entire the length of the neurite; higher ratios are indicative of greater wandering or random growth. For an average neurite that is 225 μm in length for the HMA-*co*-HDDMA series, the neurite would travel an extra 30 μm of unaligned distance, that is, outgrowth that is not in the direction of the micropattern

features, on the softest substrate with an alignment ratio of 1.32 compared to the stiffest substrate with a neurite alignment ratio of 1.18.

Because both monomers in the PEGDMA-*co*-EGDMA system undergo cross-linking reactions, tuning of the matrix stiffness is realized by modulating the ratio of the high molecular weight PEGDMA monomer relative to the low molecular weight EGDMA monomer (Figure 10A). EGDMA

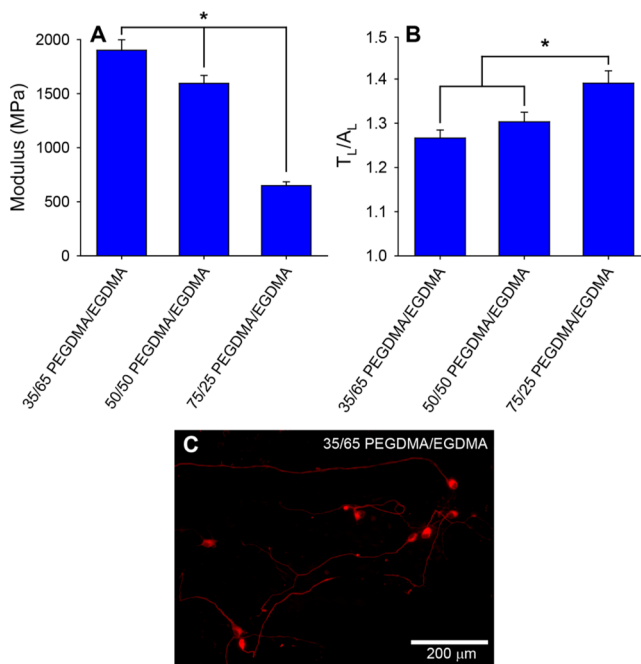


Figure 10. Modulus and SGN neurite alignment on the PEGDMA-*co*-EGDMA series. (A) Material modulus significantly decreases with increasing large PEGDMA monomer content (*, $p < 0.05$, one way ANOVA, Tukey Test). Error bars represent the SD. (B) SGN neurite alignment on the micropatterned PEGDMA-*co*-EGDMA substrates. Neurite alignment significantly increases (i.e., alignment ratio T_L/A_L decreases) with increasing substrate stiffness (*, $p < 0.05$, one way ANOVA, Dunn's Method). (C) Representative immunofluorescent image of the SGN neurite growth on the micropatterned PEGDMA-*co*-EGDMA polymers. Neurite outgrowth orients to the pattern direction that is set horizontally during the alignment measurement. Error bars represent the SE. The micropattern for each composition has a 50 μm periodicity and a 2 μm amplitude.

has the same structure as the larger PEGDMA monomer but has only one ethylene glycol repeat unit, whereas the PEGDMA monomer used for this study has ten repeat units on average. With more flexible ether repeat units between polymerizable moieties, that is, methacrylates, there are fewer cross-links per unit volume, which significantly reduces the material modulus. The material modulus for the PEGDMA-*co*-EGDMA system ranged from a maximum of 1901 ± 97 MPa to a minimum of 649 ± 35 MPa for 35 and 75 wt % PEGDMA compositions, respectively. Again, though the microfeatures were maintained at equivalent periodicity and amplitude for each composition based on the spatiotemporal reaction control afforded by photopolymerization, the SGN neurite alignment is substantially improved on the stiffer substrate compared to on the softest substrate (Figure 10B).

For many biomaterial applications that consider matrix stiffness, it is often deemed ideal to match the material modulus to that of the native tissue.^{58–60} This approach is particularly

appropriate for tissue engineering applications that aim to develop scaffolds that enable the regeneration of healthy and functional tissue. For example, isolated embryonic cardiomyocytes are shown to overstrain and stop beating on rigid substrates, beat but do little work on soft materials, and optimally strike and transmit contractile work on substrates that match the stiffness of their native matrices.⁵⁹ Potential stem cell treatments are also substantially affected by material mechanical properties since their lineage-specific differentiation has been repeatedly linked to matrix stiffness.^{62–67} Further, load bearing applications, such as cartilage tissue engineering, require the appropriate mechanical properties, that is, similar to previously lost or damaged tissue, for successful mechanical function and integration.^{60,68} However, our results demonstrate that some biomaterial applications, such as promoting spatial organization of de novo neurite growth, require a careful consideration of material mechanical property effects on cellular behavior even when the material modulus is several orders of magnitude removed from native matrix stiffness of the target tissue. Part of the physical and biomechanical signals presented to neural growth cones during development and regeneration following injury likely include interactions with high modulus native matrices of bone, that is, in the GPa range, or other dense connective tissues that are crucial to the formation of spatially organized neural networks.^{69,70} For example, SGN growth cones extend through the bony modiolus and along the osseous spiral lamina to reach the organ of Corti. While the exact mechanisms by which different cell types integrate biophysical cues remain unknown, it is evident that SGN neurites sense the matrix stiffness on materials that are much more rigid than central neural environments (e.g., brain or spinal cord) and that their alignment to biophysical cues substantially changes based on the substrate rigidity.^{71–73}

CONCLUSIONS

This work illustrates that neurite alignment to physical micropatterns is significantly affected by the matrix stiffness of the underlying network. Specifically, for both the nonpolar HMA-*co*-HDDMA and polar PEGDMA-*co*-EGDMA series, the SGN neurite alignment significantly increases when the material stiffness increases. Interestingly, neurites respond to changes in matrix stiffness that are orders of magnitude higher than what is reported for the tissue stiffness in a native neural environment. SGN survival is comparable on both methacrylate series, but the neurite length is significantly shorter on the polar PEGDMA-*co*-EGDMA substrates than on the nonpolar HMA-*co*-HDDMA substrates. Furthermore, photopolymerization is demonstrated as a powerful tool to fabricate readily tunable microfeatures across a variety of methacrylate compositions based on the spatial and temporal control of UV curing. Our results add to efforts aimed to enhance neural prosthetic performance by improving spatial signaling resolution and are also applicable to neural pathfinding and cell–material interaction applications.

AUTHOR INFORMATION

Corresponding Author

*E-mail: allan-guymon@uiowa.edu. Phone: (319)335-5015.

Notes

The authors declare no competing financial interest.

ACKNOWLEDGMENTS

The authors acknowledge funding support from the National Science Foundation (CBET-0933450) and the National Institutes of Health (NCRR-UL1RR024979, NIDCD-P30 DC010362, and NIDCD-R01 DC012578). The authors also acknowledge governmental support from the Department of Defense, Air Force Office of Scientific Research for a National Defense Science and Engineering Graduate (NDSEG) Fellowship, 32 CFR 168a.

REFERENCES

- (1) Discher, D. E.; Janmey, P.; Wang, Y. L. *Science* **2005**, *310*, 1139–1143.
- (2) Wang, Y.; Chen, C. S. *J. Cell. Mol. Med.* **2013**, *17*, 823–832.
- (3) Lo, C. M.; Wang, H. B.; Dembo, M.; Wang, Y. L. *Biophys. J.* **2000**, *79*, 144–152.
- (4) Mason, B. N.; Starchenko, A.; Williams, R. M.; Bonassar, L. J.; Reinhart-King, C. A. *Acta Biomater.* **2013**, *9*, 4635–4644.
- (5) Engler, A. J.; Sen, S.; Sweeney, H. L.; Discher, D. E. *Cell* **2006**, *126*, 677–689.
- (6) Flanagan, L. A.; Ju, Y. E.; Marg, B.; Osterfield, M.; Janmey, P. A. *NeuroReport* **2002**, *13*, 2411–2415.
- (7) Sundararaghavan, H. G.; Monteiro, G. A.; Firestein, B. L.; Shreiber, D. I. *Biotechnol. Bioeng.* **2009**, *102*, 632–643.
- (8) McKinnon, D. D.; Brown, T. E.; Kyburz, K. A.; Kiyotake, E.; Anseth, K. S. *Biomacromolecules* **2014**, *15*, 2808–2816.
- (9) Oliva, A. A.; James, C. D.; Kingman, C. E.; Craighead, H. G.; Bunker, G. A. *Neurochem. Res.* **2003**, *28*, 1639–1648.
- (10) Gustavsson, P.; Johansson, F.; Kanje, M.; Wallman, L.; Linsmeier, C. E. *Biomaterials* **2007**, *28*, 1141–1151.
- (11) Schmalenberg, K. E.; Uhrich, K. E. *Biomaterials* **2005**, *26*, 1423–1430.
- (12) Li, J.; McNally, H.; Shi, R. *J. Biomed. Mater. Res., Part A* **2008**, *87A*, 392–404.
- (13) Hurtado, A.; Cregg, J. M.; Wang, H. B.; Wendell, D. F.; Oudega, M.; Gilbert, R. J.; McDonald, J. W. *Biomaterials* **2011**, *32*, 6068–6079.
- (14) Johansson, F.; Carlberg, P.; Danielsen, N.; Montelius, L.; Kanje, M. *Biomaterials* **2006**, *27*, 1251–1258.
- (15) Miller, C.; Jeftinija, S.; Mallapragada, S. *Tissue Eng.* **2002**, *8*, 367–378.
- (16) Richardson, J. A.; Rementer, C. W.; Bruder, J. M.; Hoffman-Kim, D. *J. Neural Eng.* **2011**, *8*, 046015.
- (17) Koh, H. S.; Yong, T.; Teo, W. E.; Chan, C. K.; Puhaindran, M. E.; Tan, T. C.; Lim, A.; Lim, B. H.; Ramakrishna, S. *J. Neural Eng.* **2010**, *7*, 046003.
- (18) Yao, L.; Pandit, A.; Yao, S.; McCaig, C. D. *Tissue Eng., Part B* **2011**, *17*, 143–153.
- (19) Hoffman-Kim, D.; Mitchel, J. A.; Bellamkonda, R. V. *Annu. Rev. Biomed. Eng.* **2010**, *12*, 203–231.
- (20) Spivey, E. C.; Khaing, Z. Z.; Shear, J. B.; Schmidt, C. E. *Biomaterials* **2012**, *33*, 4264–4276.
- (21) Straley, K. S.; Foo, C. W.; Heilshorn, S. C. *J. Neurotrauma* **2010**, *27*, 1–19.
- (22) Daly, W.; Yao, L.; Zeugolis, D.; Windebank, A.; Pandit, A. *J. R. Soc., Interface* **2012**, *9*, 202–221.
- (23) O’Leary, S. J.; Richardson, R. R.; McDermott, H. J. *J. Neural Eng.* **2009**, *6*, 055002.
- (24) Leach, J. B.; Achyuta, A. K.; Murthy, S. K. *Front. Neuroeng.* **2010**, *2*, 18.
- (25) Leng, T.; Wu, P.; Mehenti, N. Z.; Bent, S. F.; Marmor, M. F.; Blumenkranz, M. S.; Fishman, H. A. *Invest. Ophthalmol. Vis. Sci.* **2004**, *45*, 4132–4137.
- (26) Winter, J. O.; Cogan, S. F.; Rizzo, J. F. *J. Biomat. Sci.-Polym. E* **2007**, *18*, 1031–1055.
- (27) Mehenti, N. Z.; Peterman, M. C.; Leng, T.; Marmor, M. F.; Blumenkranz, M. S.; Bent, S. F. *Invest. Ophthalmol. Visual Sci.* **2003**, *44*, U704–U704.

- (28) Clarke, J. C.; Tuft, B. W.; Clinger, J. D.; Levine, R.; Figueroa, L. S.; Guymon, C. A.; Hansen, M. R. *Hear. Res.* **2011**, *278*, 96–105.
- (29) Tuft, B. W.; Li, S.; Xu, L.; Clarke, J. C.; White, S. P.; Guymon, B. A.; Perez, K. X.; Hansen, M. R.; Guymon, C. A. *Biomaterials* **2013**, *34*, 42–54.
- (30) Tuft, B. W.; Xu, L.; White, S. P.; Seline, A. E.; Erwood, A. M.; Hansen, M. R.; Guymon, C. A. *ACS Appl. Mater. Interfaces* **2014**, *6*, 65–76.
- (31) Hansen, M. R.; Vijapurkar, U.; Koland, J. G.; Green, S. H. *Hear. Res.* **2001**, *161*, 87–98.
- (32) Hegarty, J.; Kay, A.; Green, S. J. *Neurosci.* **1997**, *17*, 1959–1970.
- (33) Hansen, M. R.; Bok, J.; Devaiah, A. K.; Zha, X. M.; Green, S. H. *J. Neurosci. Res.* **2003**, *72*, 169–184.
- (34) Hansen, M. R.; Zha, X. M.; Bok, J.; Green, S. H. *J. Neurosci.* **2001**, *21*, 2256–2267.
- (35) Roehm, P. C.; Xu, N.; Woodson, E. A.; Green, S. H.; Hansen, M. R. *Mol. Cell. Neurosci.* **2008**, *37*, 376–387.
- (36) Bryant, S. J.; Hauch, K. D.; Ratner, B. D. *Macromolecules* **2006**, *39*, 4395–4399.
- (37) Bryant, S. J.; Cuy, J. L.; Hauch, K. D.; Ratner, B. D. *Biomaterials* **2007**, *28*, 2978–2986.
- (38) Abbe, E. *Arch. Mikrosk. Anat.* **1873**, *9*, 413–468.
- (39) Garini, Y.; Vermolen, B. J.; Young, I. T. *Curr. Opin. Biotechnol.* **2005**, *16*, 3–12.
- (40) Smith, D. M.; Li, C. Y.; Bunning, T. J. *J. Polym. Sci., Part B: Polym. Phys.* **2014**, *52*, 232–250.
- (41) Wright, A.; Davis, A.; Bredberg, G.; Ulehlova, L.; Spencer, H.; Bock, G.; Felix, H.; Iurato, S.; Johnsson, L. G.; Paufer, M. *Acta Otolaryngol.* **1987**, 1–48.
- (42) Singh, A. V.; Patil, R.; Thombre, D. K.; Gade, W. N. *J. Biomed. Mater. Res., Part A* **2013**, *101*, 3019–3032.
- (43) Schmidt, R. C.; Healy, K. E. *J. Biomed. Mater. Res., Part A* **2009**, *90A*, 1252–1261.
- (44) Diehl, K. A.; Foley, J. D.; Nealey, P. F.; Murphy, C. J. *J. Biomed. Mater. Res., Part A* **2005**, *75A*, 603–611.
- (45) Charest, J. M.; Califano, J. P.; Carey, S. P.; Reinhart-King, C. A. *Macromol. Biosci.* **2012**, *12*, 12–20.
- (46) Chou, C.; Rivera, A. L.; Sakai, T.; Caplan, A. I.; Goldberg, V. M.; Welter, J. F.; Baskaran, H. *Tissue Eng., Part A* **2013**, *19*, 1081–1090.
- (47) Tawfick, S.; De Volder, M.; Copic, D.; Park, S. J.; Oliver, C. R.; Polsen, E. S.; Roberts, M. J.; Hart, A. J. *Adv. Mater.* **2012**, *24*, 1628–1674.
- (48) Arima, Y.; Iwata, H. *Biomaterials* **2007**, *28*, 3074–3082.
- (49) Göbbels, K.; Kuenzel, T.; van Ooyen, A.; Baumgartner, W.; Schnakenberg, U.; Bräunig, P. *Biomaterials* **2010**, *31*, 1055–1067.
- (50) Lee, J. H.; Lee, J. W.; Khang, G.; Lee, H. B. *Biomaterials* **1997**, *18*, 351–358.
- (51) Tamada, Y.; Ikada, Y. *Polymer* **1993**, *34*, 2208–2212.
- (52) Nurcombe, V. *Pharmacol. Ther.* **1992**, *56*, 247–264.
- (53) Norde, W.; Horbett, T. A.; Brash, J. L. *Proteins at Interfaces III: Introductory Overview*; American Chemical Society: Washington, DC, 2012; Vol. 1120, pp 134.
- (54) Palchesko, R. N.; Zhang, L.; Sun, Y.; Feinberg, A. W. *PLoS One* **2012**, *7*, e51499.
- (55) Lampe, K. J.; Antaris, A. L.; Heilshorn, S. C. *Acta Biomater.* **2013**, *9*, 5590–5599.
- (56) Chou, S.; Cheng, C.; Chen, C.; LeDuc, P. R. *Soft Matter* **2011**, *7*, 9871–9877.
- (57) Leach, J. B.; Brown, X. Q.; Jacot, J. G.; DiMilla, P. A.; Wong, J. Y. *J. Neural Eng.* **2007**, *4*, 26–34.
- (58) Moglia, R. S.; Robinson, J. L.; Muschenborn, A. D.; Touchet, T. J.; Maitland, D. J.; Cosgriff-Hernandez, E. *Polymer* **2014**, *55*, 426–434.
- (59) Engler, A. J.; Carag-Krieger, C.; Johnson, C. P.; Raab, M.; Tang, H.; Speicher, D. W.; Sanger, J. W.; Sanger, J. M.; Discher, D. E. *J. Cell. Sci.* **2008**, *121*, 3794–3802.
- (60) Kemppainen, J. M.; Hollister, S. J. *J. Biomed. Mater. Res., Part A* **2010**, *94A*, 9–18.
- (61) Yu, T. T.; Shoichet, M. S. *Biomaterials* **2005**, *26*, 1507–1514.
- (62) Engler, A. J.; Sen, S.; Sweeney, H. L.; Discher, D. E. *Cell* **2006**, *126*, 677–689.
- (63) Wang, Y.; Chen, C. S. *J. Cell. Mol. Med.* **2013**, *17*, 823–832.
- (64) Ayala, R.; Zhang, C.; Yang, D.; Hwang, Y.; Aung, A.; Shroff, S. S.; Arce, F. T.; Lal, R.; Arya, G.; Varghese, S. *Biomaterials* **2011**, *32*, 3700–3711.
- (65) Kim, I. L.; Khetan, S.; Baker, B. M.; Chen, C. S.; Burdick, J. A. *Biomaterials* **2013**, *34*, 5571–5580.
- (66) Engler, A. J.; Griffin, M. A.; Sen, S.; Bonnetmann, C. G.; Sweeney, H. L.; Discher, D. E. *J. Cell Biol.* **2004**, *166*, 877–887.
- (67) Park, J. S.; Chu, J. S.; Tsou, A. D.; Diop, R.; Tang, Z.; Wang, A.; Li, S. *Biomaterials* **2011**, *32*, 3921–3930.
- (68) Xiao, Y.; Friis, E. A.; Gehrke, S. H.; Detamore, M. S. *Tissue Eng., Part B* **2013**, *19*, 403–412.
- (69) Rho, J. Y.; Ashman, R. B.; Turner, C. H. *J. Biomech.* **1993**, *26*, 111–119.
- (70) Zysset, P. K.; Guo, X. E.; Hoffler, C. E.; Moore, K. E.; Goldstein, S. A. *J. Biomech.* **1999**, *32*, 1005–1012.
- (71) Lewis, K. J.; Anseth, K. S. *MRS Bull.* **2013**, *38*, 260–268.
- (72) Eyckmans, J.; Boudou, T.; Yu, X.; Chen, C. S. *Dev. Cell* **2011**, *21*, 35–47.
- (73) Chen, C. S. *J. Cell. Sci.* **2008**, *121*, 3285–3292.